Carbonate assemblages in Cold Bokkeveld CM chondrite reveal complex parent body evolution

The Meteoritical Society

Meteoritics & Planetary Science 1–19 (2021)
doi: 10.1111/maps.13647

Carbonate assemblages in Cold Bokkeveld CM chondrite reveal complex parent body evolution

Stefan FARSANG[1*], Ian A. FRANCHI[2], Xuchao ZHAO[2], Timothy D. RAUB[3], Simon A.T. REDFERN[4], and Monica M. GRADY[2,5]

[1]Department of Earth Sciences, University of Cambridge, Downing Street, Cambridge CB2 3EQ, UK
[2]School of Physical Sciences, The Open University, Walton Hall, Milton Keynes MK7 6AA, UK
[3]School of Earth & Environmental Sciences, University of St Andrews, Irvine Building, St Andrews KY16 9AL, UK
[4]Asian School of the Environment, Nanyang Technological University, 50 Nanyang Avenue, Singapore 639798, Singapore
[5]Department of Earth Sciences, Natural History Museum, Cromwell Rd, London SW7 5BD, UK
[*]Corresponding author. E-mail: sf571@cam.ac.uk

(Received 18 September 2020; revision accepted 26 February 2021)

Abstract–The paragenesis of carbonates in the Cold Bokkeveld CM chondrite is determined from a detailed petrographic, chemical, spectroscopic, and isotopic study of nine associations of carbonates (aragonite, calcite, and dolomite) with other secondary minerals that occur within the meteorite. Our study reveals the existence of carbonates displaying petrographic features that are distinct from those of type 1 and type 2 carbonates commonly observed in CM2 meteorites. These include carbonates interstitial to octahedral magnetite crystals, for which a new designation of "type 1c" is suggested. The O isotopic values of dolomite ($\delta^{18}O$ ranging from +21.1 to +25.8‰ and $\Delta^{17}O$ from −4.9 to −4.0‰) are similar to those measured in dolomites from other CM chondrites. The presence of complex carbonates with a $CaCO_3$ core and Mg-enriched rim implies several generations of fluids and/or their evolving composition on the CM parent body(ies). Petrographic characteristics indicate at least six stages of potentially overlapping carbonate and phyllosilicate formation events. We show that type 1 and type 2 calcite have distinct Raman spectral characteristics. Type 1 calcite is characterized by very broad peaks, whereas type 2 calcite displays narrow peaks similar to those of typical abiotic terrestrial calcite, suggesting high crystallinity. A carbonate Raman spectrum showing features characteristic of both aragonite and calcite likely documents an aragonite-calcite phase transition. Raman spectroscopy also reveals the presence of organic matter in the majority of carbonates. This indicates that organic carbon was mobilized by aqueous fluids for extended periods.

INTRODUCTION

Carbonaceous chondrite meteorites represent some of the most primitive materials formed in the early solar system. CM chondrites are the most abundant and diverse group of carbonaceous chondrites and experienced various degrees of brecciation, aqueous alteration, and metamorphic heating. Some moderately altered CM2 chondrites, including Cold Bokkeveld, Jbilet Winselwan, and Nogoya, are highly complex impact breccias that contain lithic clasts and mineral fragments showing various degrees of aqueous alteration (Bischoff et al. 2017; Lentfort et al. 2020; Zolensky et al. 2020). Their sub-mm-scale heterogeneity and petrographic features point toward major pre-accretionary aqueous alteration on small precursor planetesimals, followed by large-scale parent body aqueous alteration (Bischoff 1998; Bischoff et al. 2017). In contrast, the lower degree of inter- and intrasample heterogeneity in highly altered CM1 chondrites presumably attests to more extensive parent body alteration overprinting much of the inherited, pre-accretionary alteration features.

Carbonate minerals in CM chondrites are good indicators of secondary processing as they are thought to be products of aqueous alteration in the CM parent

body(ies) (e.g., McSween 1979; Grady et al. 1988; Johnson and Prinz 1993; Riciputi et al. 1994; Brearley et al. 1999; Brearley and Hutcheon 2002; Benedix et al. 2003; Guo and Eiler 2007; Lindgren et al. 2011, 2017; Tyra et al. 2012; Lee et al. 2013, 2014; Alexander et al. 2015; Chan et al. 2017; Verdier-Paoletti et al. 2017; Telus et al. 2019). They precipitated from aqueous fluids and their elemental compositions and isotopic signatures are widely used to reconstruct fluid composition and formation temperatures (Johnson and Prinz 1993; Riciputi et al. 1994; Benedix et al. 2003; Guo and Eiler 2007; Lee et al. 2013, 2014; Alexander et al. 2015; Lindgren et al. 2017; Verdier-Paoletti et al. 2017; Telus et al. 2019). Carbonates are minor phases in CM chondrites, with modal abundances variously estimated from 1.4 ± 0.2 to 2.8 ± 0.6 vol% (de Leuw et al. 2010) or <0.1 to 2.3 vol% (Lee et al. 2014). Carbonates reported from CM chondrites include aragonite and calcite (both polymorphs of $CaCO_3$), dolomite ($Ca,Mg[CO_3]_2$) and breunnerite ($[Mg,Fe]CO_3$), a ferroan magnesite (Lee et al. 2014). Based on petrographic features, calcite grains in CM chondrites have been classified into type 1, type 2, and type 3 grains, with type 3 being vein-infill grains formed as a result of terrestrial weathering processes (Tyra et al. 2007, 2012). Each of the type 1 and type 2 grains was later subdivided into two varieties (Lee et al. 2014): type 1a are subhedral or anhedral crystals or equant grains, typically <~70 μm in size, usually with serpentine/tochilinite rims. They are often twinned, may show zoning in cathodoluminescence (CL), and can contain bands of nanopores (pores much smaller than 100 nm). Type 1b grains are similar to type 1a, but lack the serpentine/tochilinite rims and nanopores, and are instead intergrown with coarse Fe-sulfide or Fe–Ni-sulfide crystals. Type 2 grains are finely polycrystalline and microporous (pores larger than 100 nm) and lack the serpentine/tochilinite rims. Type 2a grains characteristically contain few micrometer-size Fe–Ni-sulfide inclusions, whereas type 2b grains are free of sulfides. In CM2.1 and CM2.0 meteorites, calcite intergrown with dolomite and/or breunnerite has also been found (Lee et al. 2014).

Cold Bokkeveld is an impact regolith breccia (Lee 1993) that shows significant inter- and intrasample mineralogical heterogeneity (Beck et al. 2010) and was therefore chosen as the target meteorite for this study. It was originally classified as a 2.2 CM chondrite (Rubin et al. 2007), but because its clasts experienced various degrees of aqueous alteration, new classifications of CM2.1–2.6 (Bischoff et al. 2017) and CM2.1–2.7 (Lentfort et al. 2020) have been suggested. The modal mineralogy of Cold Bokkeveld bulk sample, determined by X-ray diffraction (Howard et al. 2009, 2011), comprises serpentine (54.1 vol%), cronstedtite (23.3 vol%), olivine (11.5 vol%), pyroxene (4.9 vol%), sulfides (3.0 vol%), magnetite (2.0 vol%), calcite (1.0 vol%), and gypsum (0.8 vol%). Other estimates of the carbonate fraction in Cold Bokkeveld are 1.9 ± 0.2 vol% (de Leuw et al. 2010) and 1.8 vol% (Lee et al. 2014). Carbonate species described in Cold Bokkeveld include aragonite (Barber 1981; Lee et al. 2014), calcite (Barber 1981; Johnson and Prinz 1993; Lee 1993; Howard et al. 2009, 2011; Lee et al. 2014), an undefined Ca-carbonate (Benedix et al. 2003; Rubin et al. 2007; de Leuw et al. 2010), and sporadic dolomite (Johnson and Prinz 1993; Benedix et al. 2003). Here, we emphasize the difficulty in distinguishing between $CaCO_3$ polymorphs occurring in chondrites (aragonite and calcite, respectively) based on chemical analysis and preview our employment of a complementary technique (i.e., Raman spectroscopy).

Petrographic characteristics revealed up to two carbonate-forming events operating on the parent body of Cold Bokkeveld (Lee et al. 2014); the oxygen isotopic compositions of the carbonates have been employed to determine their formation temperatures. Carbonate clumped isotope thermometry yielded carbonate formation temperatures for separate Cold Bokkeveld aliquots of ~26, ~35, and ~71 °C (Guo and Eiler 2007), consistent with the relatively low temperature alteration of CM2 chondrites inferred from C and O isotopic compositions (e.g., Alexander et al. 2015). However, the novel method of Verdier-Paoletti et al. (2017) gave much higher carbonate formation temperatures ranging from 97.9 to 225.3 °C. Clumped isotopes have also been used to infer basic conditions with a minimum pH value of 11.7 during carbonate formation (Guo and Eiler 2007).

Despite the broad literature on CM chondritic carbonate minerals, the paragenetic sequence of carbonates and associated phases on the CM chondrite parent body is not fully understood. We present a combined petrographic, chemical, spectroscopic, and isotopic study of nine carbonate assemblages in Cold Bokkeveld in order to determine the alteration processes associated with their formation and to reconstruct their formation sequence. These carbonates are found in association with pyrrhotite ($Fe_{[1-x]}S$ [$x = 0$–0.17]), pentlandite ($[Fe,Ni]_9S_8$–, tochilinite (6Fe0.9S·5[Mg,Fe][$(OH]_2$), magnetite ($Fe^{2+}Fe_2{}^{3+}O_4$), and phyllosilicates.

METHODS

Scanning Electron Microscopy

A FEI Quanta 650F instrument equipped with two Bruker XFlash 6|30 silicon drift EDX detectors and a Deben Centaurus CL detector with a wide range (185–850 nm) scintillator at the Department of Earth

Sciences, University of Cambridge was employed for secondary electron (SE), back-scattered electron (BSE), and CL imaging, and for qualitative chemical analysis using energy-dispersive spectroscopy (EDS). All analyses were done on a carbon coated thin section under high-vacuum conditions.

SE and BSE images were collected using an accelerating voltage of 20 keV and a working distance of 13 mm. CL images were obtained using an accelerating voltage of 5 keV, a working distance of 11.4 mm, and a dwell time of 100 μs. EDS element maps were collected using an accelerating voltage of 20 keV, a working distance of 13 mm, and an acquisition time of 10–20 min.

Electron Probe Microanalysis

A CAMECA SX-100 microprobe with five wavelength dispersive spectrometers at the Department of Earth Sciences, University of Cambridge was used for quantitative chemical analysis.

Carbonates were analyzed using a beam diameter of 2 μm. For Na and Ca analysis, an accelerating voltage of 15 keV and a beam current of 4 nA was used, while for Mg, Si, Cr, Mn, Fe, Ni, and Sr, an accelerating voltage of 15 keV and a beam current of 20 nA was used. Standards included jadeite for Na, periclase for Mg, diopside for Si and Ca, Cr-metal for Cr, Mn-metal for Mn, fayalite for Fe, Ni-metal for Ni, and celestine for Sr. Typical detection limits (in wt%) were Na (0.08), Mg (0.01), Si (0.02), Ca (0.23), Cr (0.03), Mn (0.04), Fe (0.04), Ni (0.06), and Sr (0.04). The amount of CO_2 was calculated assuming stoichiometric compositions of carbonates containing all Mg, Ca, Fe, Mn, and Sr detected.

Sulfides were analyzed using a beam diameter of 1 μm. For Mg, Si, P, S, Cl, Ca, Ti, Cr, Mn, Fe, Co, Ni, Cu, and Zn, an accelerating voltage of 15 keV and a beam current of 20 nA was used. Standards included olivine for Mg, diopside for Si and Ca, apatite for P, pyrite for S, halite for Cl, rutile for Ti, Cr-metal for Cr, Mn-metal for Mn, fayalite for Fe, Co-metal for Co, Ni-metal for Ni, Cu-metal for Cu, and Zn-metal for Zn. Typical detection limits (in wt%) were Mg (0.02), Si (0.02), P (0.02), S (0.10), Cl (0.02), Ca (0.03), Ti (0.02), Cr (0.07), Mn (0.10), Fe (0.21), Co (0.10), Ni (0.12), Cu (0.14), and Zn (0.20).

Raman Spectroscopy

Raman spectra were collected across the 100–1800 cm^{-1} spectral range using a confocal LabRAM 300 (Horiba Jobin Yvon) Raman spectrometer with 300 mm focal length objective, at the Department of Earth Sciences, University of Cambridge. A holographic grating of 1800 g mm^{-1} coupled to a Peltier front-illuminated CCD detector (1024 × 256 pixels in size) enabled a spectral resolution of ~1 cm^{-1}. The excitation line at 532.05 nm was produced by a Ventus 532 laser source (Laser Quantum) operated at 100 mW at the source and focused on the sample using an Olympus LMPLFLN 50× long working distance objective. The spot size was ~1 μm and for each spot, five accumulations of spectra, each with 20 s exposure time, were obtained, resulting in a total acquisition time of 100 s.

All Raman spectra were treated by PeakFit software. For each Raman spectrum, the baseline was subtracted, and peak features were determined by least squares fitting to Voigt profiles for each Raman peak/band. Peak positions were calibrated against the measured excitation of a Ne light emission reference spectrum (Saloman and Sansonetti 2004).

Secondary Ion Mass Spectroscopy

Oxygen isotopic composition was measured by a CAMECA Nano Secondary Ion Mass Spectrometry (NanoSIMS) 50L instrument at the School of Physical Sciences, The Open University. The analyses were conducted by rastering a focused Cs^+ primary ion beam with a current of ~50 pA over the areas of interest. Before analysis, a current of ~150 pA was used for implanting Cs^+ ions evenly and pre-sputtering the gold coating and possible surface contamination across the areas of interest. Secondary ions were collected simultaneously, with ^{16}O on a Faraday cup, and ^{17}O, ^{18}O, ^{28}Si, $^{24}Mg^{16}O$, $^{40}Ca^{16}O$, and $^{56}Fe^{16}O$ on electron multipliers. $^{24}Mg^{16}O$, $^{40}Ca^{16}O$, and $^{56}Fe^{16}O$ were monitored to avoid contributions from inclusions and surrounding phases. The mass resolving power was set to >10,000 (CAMECA definition, based on the measured peak width between 10% and 90% of the peak), which was sufficient to resolve the interference of ^{16}OH from the ^{17}O peak. An electron gun was used for charge compensation. Crack- and contamination-free areas were chosen for NanoSIMS analysis. The measured areas had dimensions of 5 × 5 μm, while pre-sputtering was done on areas of 7 × 7 μm. Analysis times were ~6 min with ~2 min pre-sputtering. The total count of ^{16}O in a single measurement was ~9×10^9. Oxygen isotope variations are expressed in delta notation, i.e., in ‰ units relative to a bracketing standard. For $\delta^{17}O$ and $\delta^{18}O$ (‰ versus standard mean ocean water):

$$\delta^x O = \left(\frac{[^xO/^{16}O]_{sample}}{[^xO/^{16}O]_{SMOW}} - 1 \right) \times 1000$$

The departure from the terrestrial fractionation line is quantified using $\Delta^{17}O$ or ^{17}O-excess:

$$\Delta^{17}O = \delta^{17}O - 0.52 \times \delta^{18}O$$

Instrumental mass fractionation (IMF) effects were calibrated with measurements, before and after measuring the unknown samples, of a dolomite standard provided by the Natural History Museum, London. Sample BM1982,189 (from near Legananam Pot, Dungiven, County Londonderry, UK) has a composition of $\delta^{18}O = 20.0 \pm 1.0‰$ and inferred $\delta^{17}O = 10.4 \pm 1.6‰$. An additional IMF correction was applied to the Cold Bokkeveld samples to account for the discrepancy in the Fe + Mn concentration compared to the abundance in the standard. The detailed calibration for the matrix effect for varying Fe in dolomite-ankerite solution series has been reported by Śliwiński et al. (2016), and is essentially identical to an earlier study undertaken using the Open University NanoSIMS (Tomkinson 2013). While neither study considered the effects of Mn in isolation, the effects of Mn are considered comparable to that of Fe, and therefore to account for the high abundance of Mn in the samples the correction was applied using the approach of Śliwiński et al. (2016) using abundance of Fe + Mn instead of just Fe. The standard used has an Fe# (= [Fe + Mn]/[Fe + Mn+Mg]) of 0.12 while the samples range from 0.17 to 0.24. The mean value of 0.19 results in an additional matrix correction of 1.5‰ for $\delta^{18}O$ following the calibration of Śliwiński et al. (2016). And while the specific composition of the individual spots analyzed by NanoSIMS is unknown, the observed range in Fe# is small, resulting in a variation of matrix correction of only ±0.5‰. Given the uncertainties in the measurements and the range of oxygen isotopic compositions, the additional corrections for Fe + Mn variation in the samples are negligible and only the correction for the average composition has been applied. As matrix effects are entirely mass dependent, the matrix effect on the $\delta^{17}O$ values was applied in a mass-dependent manner.

The 2σ uncertainties for the NanoSIMS measurements were generated by combining internal errors for each analysis with the standard deviation of the mean of the corresponding standards.

RESULTS

Natural History Museum, London thin section Cold Bokkeveld P5449 from sample BM.1727 was searched for the presence of carbonate minerals. Nine carbonate assemblages showing different petrographic characteristics were systematically studied. In these, three carbonate minerals were identified by the combination of SEM, EPMA, and Raman spectroscopy: aragonite, calcite, and dolomite.

Petrography and Chemistry

Here, we provide a petrographic description of the individual carbonate assemblages. These originate from a number of clasts showing different degrees of aqueous alteration. Results of chemical analysis of carbonates and those of the associated sulfides are summarized in Tables 1 and 2, respectively.

Assemblage 1 is a globular ~25 × 30 μm object with well-defined boundaries embedded in a phyllosilicate and tochilinite-rich matrix (Figs. 1a and 1b). In this object, P-bearing (0.28 wt%, $n = 1$) pentlandite is uniformly distributed in interstitial carbonate. The carbonate object has a speckled appearance in reflected light as opposed to the highly reflective nature of type 1 and type 2 carbonates (see below). The object has a $CaCO_3$ (likely calcitic) core and Mg-enriched (likely dolomitic) rim.

Assemblage 2 is an irregular ~300 × 450 μm object embedded in a phyllosilicate-rich matrix (Figs. 1c and 1d). In this object, hundreds of uniformly distributed P-rich (4.48–5.40 wt%, $n = 3$) and Cr-rich (1.24–3.79 wt%, $n = 3$) pentlandite clasts occur in interstitial $CaCO_3$. The $CaCO_3$ has a speckled appearance in reflected light and some of it has been replaced by tochilinite.

Assemblage 3 is a globular ~100 × 130 μm object embedded in a phyllosilicate-rich matrix (Figs. 1e and 1f). It comprises a pyrrhotite crystal with a pentlandite rim, which is partially replaced by calcite along the pyrrhotite/pentlandite boundary. Some of the pyrrhotite that is in direct contact with pentlandite and calcite is altered to magnetite. The morphology of the pyrrhotite/pentlandite grain (uniformly oriented crystal remnants at the pyrrhotite/pentlandite boundary) indicates that its partial dissolution had a crystallographic control.

Assemblage 4 comprises two globular calcite crystals with tochilinite rims and an aragonite crystal, embedded in a phyllosilicate-rich matrix (Figs. 2a and 2b). While the larger calcite crystal is relatively pure and inclusion-free, the other contains numerous sub-micrometer sulfide inclusions visible on the Ni element map. Chemical analysis of this calcite crystal shows the presence of Cr, Fe, and Ni (Table 1). The globular shape of calcite crystals (resembling a chondrule) and the presence of micrometer-size sulfide inclusions is consistent with type 2a calcite (Lee et al. 2014). Abundant type 2 carbonate occurring as pseudomorphs replacing chondrule silicate minerals was also reported in the Nogoya CM2 chondrite (Benedix et al. 2003).

Table 1. Chemical composition of carbonates in Cold Bokkeveld CM chondrite.

Na_2O	MgO	SiO_2	CaO	Cr_2O_3	MnO	FeO	NiO	SrO	CO_2	Total
Assemblage 2 ($CaCO_3$)										
b.d.l.	b.d.l.	0.07	55.06	0.07	b.d.l.	0.71	0.35	b.d.l.	43.65	99.91
b.d.l.	b.d.l.	0.11	55.44	0.05	b.d.l.	0.58	0.30	b.d.l.	43.89	100.37
b.d.l.	b.d.l.	0.14	54.90	0.07	b.d.l.	0.58	0.49	b.d.l.	43.45	99.63
Assemblage 3 (calcite)										
0.12	b.d.l.	0.08	55.01	b.d.l.	b.d.l.	1.03	0.14	b.d.l.	43.80	100.18
0.14	b.d.l.	0.08	55.10	b.d.l.	b.d.l.	1.26	b.d.l.	b.d.l.	44.02	100.60
0.14	b.d.l.	0.10	54.44	b.d.l.	b.d.l.	1.81	0.10	b.d.l.	43.84	100.43
Assemblage 4 (calcite)										
0.16	0.14	0.45	54.92	0.03	b.d.l.	0.61	b.d.l.	b.d.l.	43.64	99.95
0.08	b.d.l.	0.13	52.96	1.25	b.d.l.	1.33	1.06	b.d.l.	42.40	99.21
0.11	b.d.l.	0.07	53.32	1.56	b.d.l.	1.40	1.32	b.d.l.	42.71	100.49
Assemblage 6 (calcite)										
b.d.l.	b.d.l.	0.04	55.24	b.d.l.	b.d.l.	0.56	b.d.l.	b.d.l.	43.70	99.54
b.d.l.	b.d.l.	b.d.l.	55.68	b.d.l.	b.d.l.	0.45	b.d.l.	b.d.l.	43.99	100.12
b.d.l.	b.d.l.	0.03	55.43	b.d.l.	b.d.l.	0.54	b.d.l.	b.d.l.	43.83	99.83
Assemblage 7 (calcite)										
b.d.l.	b.d.l.	0.13	54.94	b.d.l.	b.d.l.	0.67	0.10	b.d.l.	43.53	99.37
b.d.l.	b.d.l.	0.17	55.24	b.d.l.	b.d.l.	1.04	0.08	b.d.l.	43.99	100.52
b.d.l.	b.d.l.	0.10	55.63	b.d.l.	b.d.l.	0.79	0.08	b.d.l.	44.15	100.75
Assemblage 8 (dolomite)										
b.d.l.	17.77	0.04	28.48	b.d.l.	4.31	3.44	b.d.l.	b.d.l.	46.55	100.59
b.d.l.	18.67	0.05	28.45	b.d.l.	3.41	3.19	b.d.l.	b.d.l.	46.78	100.55
b.d.l.	16.72	0.43	29.93	b.d.l.	4.26	2.36	b.d.l.	0.06	45.85	99.61
b.d.l.	17.94	0.04	29.17	b.d.l.	3.59	3.15	b.d.l.	b.d.l.	46.64	100.53
b.d.l.	17.70	0.25	28.50	b.d.l.	3.87	3.19	b.d.l.	b.d.l.	46.05	99.56
b.d.l.	16.10	0.14	29.08	b.d.l.	5.18	3.76	b.d.l.	b.d.l.	45.93	100.19

All values are in wt%. b.d.l. = below detection limit

Table 2. Chemical composition of sulfides associated with carbonates in Cold Bokkeveld CM chondrite.

Mg	Si	P	S	Cl	Ca	Ti	Cr	Mn	Fe	Co	Ni	Cu	Zn	Total
Assemblage 1														
0.70	0.70	0.28	31.12	0.02	1.07	b.d.l.	b.d.l.	b.d.l.	29.76	1.54	28.49	b.d.l.	b.d.l.	93.68
Assemblage 2														
0.08	0.12	5.40	21.35	0.09	1.2	b.d.l.	1.24	b.d.l.	23.89	1.79	31.68	b.d.l.	b.d.l.	86.84
0.14	0.13	4.96	22.03	0.07	1.54	b.d.l.	2.85	b.d.l.	23.16	2.34	31.65	b.d.l.	b.d.l.	88.87
0.09	0.06	4.48	25.16	0.06	0.25	b.d.l.	3.79	b.d.l.	27.45	1.69	30.26	b.d.l.	b.d.l.	93.29
Assemblage 3														
b.d.l.	b.d.l.	b.d.l.	37.47	b.d.l.	b.d.l.	b.d.l.	b.d.l.	b.d.l.	59.13	0.26	1.85	b.d.l.	b.d.l.	98.71
b.d.l.	b.d.l.	b.d.l.	38.14	b.d.l.	0.04	b.d.l.	b.d.l.	b.d.l.	58.93	0.21	1.84	b.d.l.	b.d.l.	99.16
b.d.l.	b.d.l.	b.d.l.	38.8	b.d.l.	0.06	b.d.l.	b.d.l.	b.d.l.	58.64	0.25	1.97	b.d.l.	b.d.l.	99.72
0.05	0.07	b.d.l.	34.05	b.d.l.	0.23	b.d.l.	b.d.l.	b.d.l.	31.87	1.29	31.4	b.d.l.	b.d.l.	98.96
Assemblage 5														
0.16	0.18	b.d.l.	33.44	b.d.l.	0.04	b.d.l.	b.d.l.	b.d.l.	33.31	0.73	30.2	b.d.l.	b.d.l.	98.06
Assemblage 7														
0.02	0.04	b.d.l.	33.08	b.d.l.	b.d.l.	b.d.l.	0.07	b.d.l.	30.16	2.37	33.36	b.d.l.	b.d.l.	99.10
Assemblage 8														
b.d.l.	b.d.l.	b.d.l.	37.95	b.d.l.	b.d.l.	b.d.l.	b.d.l.	b.d.l.	61.15	b.d.l.	0.31	b.d.l.	b.d.l.	99.41
b.d.l.	0.04	b.d.l.	38.23	b.d.l.	0.22	b.d.l.	b.d.l.	b.d.l.	60.18	b.d.l.	0.33	b.d.l.	b.d.l.	99.00
b.d.l.	0.03	b.d.l.	37.23	b.d.l.	0.12	b.d.l.	b.d.l.	b.d.l.	61.44	b.d.l.	0.34	b.d.l.	b.d.l.	99.16

All values are in wt%. b.d.l. = below detection limit

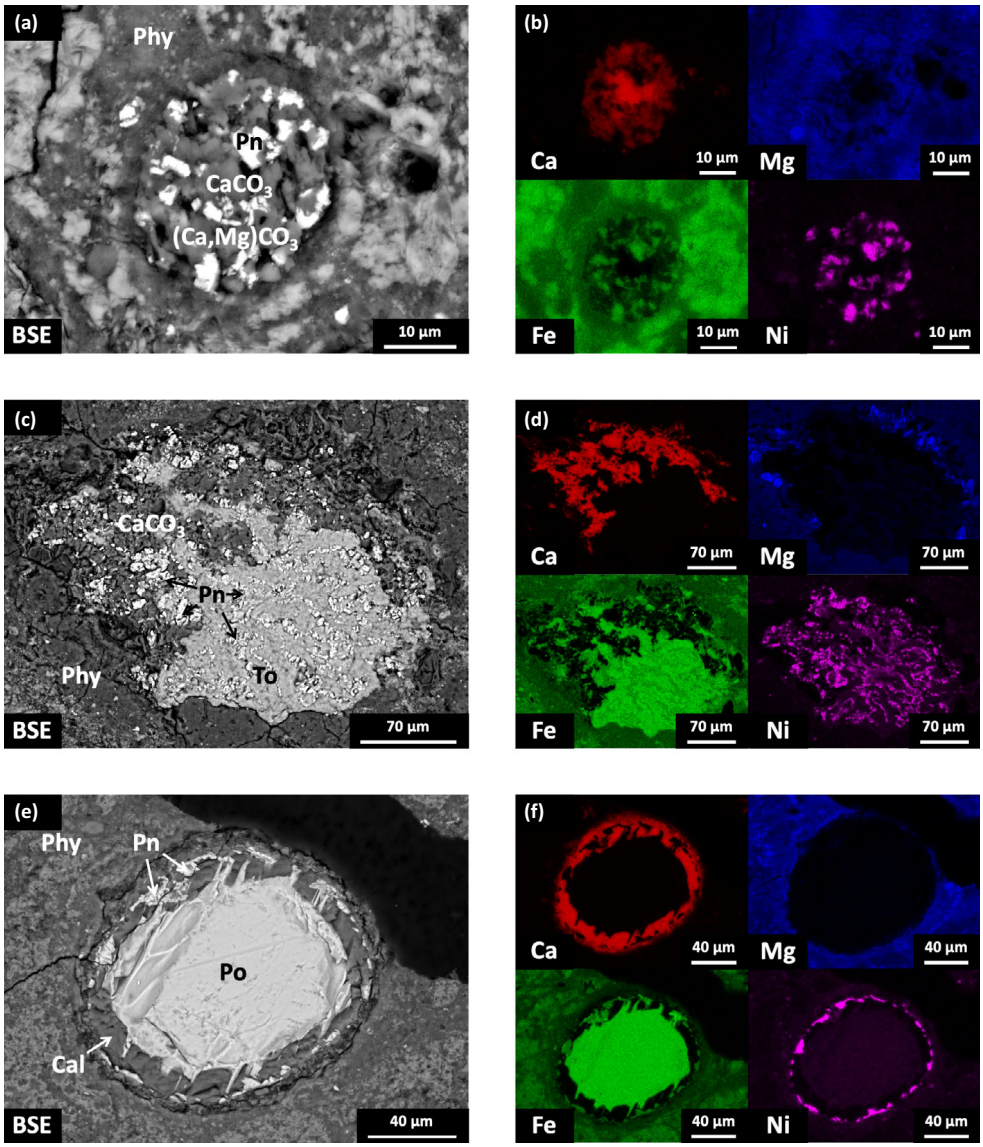

Fig. 1. a, b) BSE image and EDS element maps of assemblage 1: pentlandite (Pn) with interstitial carbonate embedded in phyllosilicate-rich (Phy) matrix. c, d) BSE image and EDS element maps of assemblage 2: pentlandite (Pn) with interstitial $CaCO_3$ and tochilinite (To) embedded in phyllosilicate-rich (Phy) matrix. e, f) BSE image and EDS element maps of assemblage 3: pyrrhotite (Po) surrounded by calcite (Cal) and pentlandite (Pn) embedded in phyllosilicate-rich (Phy) matrix.

Assemblages 5 and 6 comprise euhedral calcite crystals surrounded by tochilinite, embedded in a phyllosilicate-rich matrix (Figs. 2c and 2d). The tochilinite in Fig. 2c is in contact with pentlandite. These euhedral calcite crystals represent type 1a calcite formed by cementation of fluid-filled pore space (Lee et al. 2014). After the growth of these into the pores, the remaining porosity between the calcite crystals and walls was filled with tochilinite (Lee et al. 2014).

Assemblage 7 consists of subhedral calcite crystals in close proximity to a pentlandite grain, embedded in a phyllosilicate-rich matrix (Figs. 2e and 2f). These subhedral crystals represent type 1b calcite formed by cementation of fluid-filled pore space (Lee et al. 2014). In contrast to 1a calcite, they lack tochilinite and/or phyllosilicate rim (Lee et al. 2014).

Assemblage 8 contains a ~1.1 × 0.6 mm calcite-rich chondrule pseudomorph, in which type 1a calcite and dolomite are often in contact with one another and with tabular pyrrhotite crystals (Fig. 3). The clast also contains abundant phyllosilicates and minor pentlandite. Whereas the central part of the assemblage is richer in calcite grains, there are more dolomite crystals at the edges. Dolomite also forms rims around

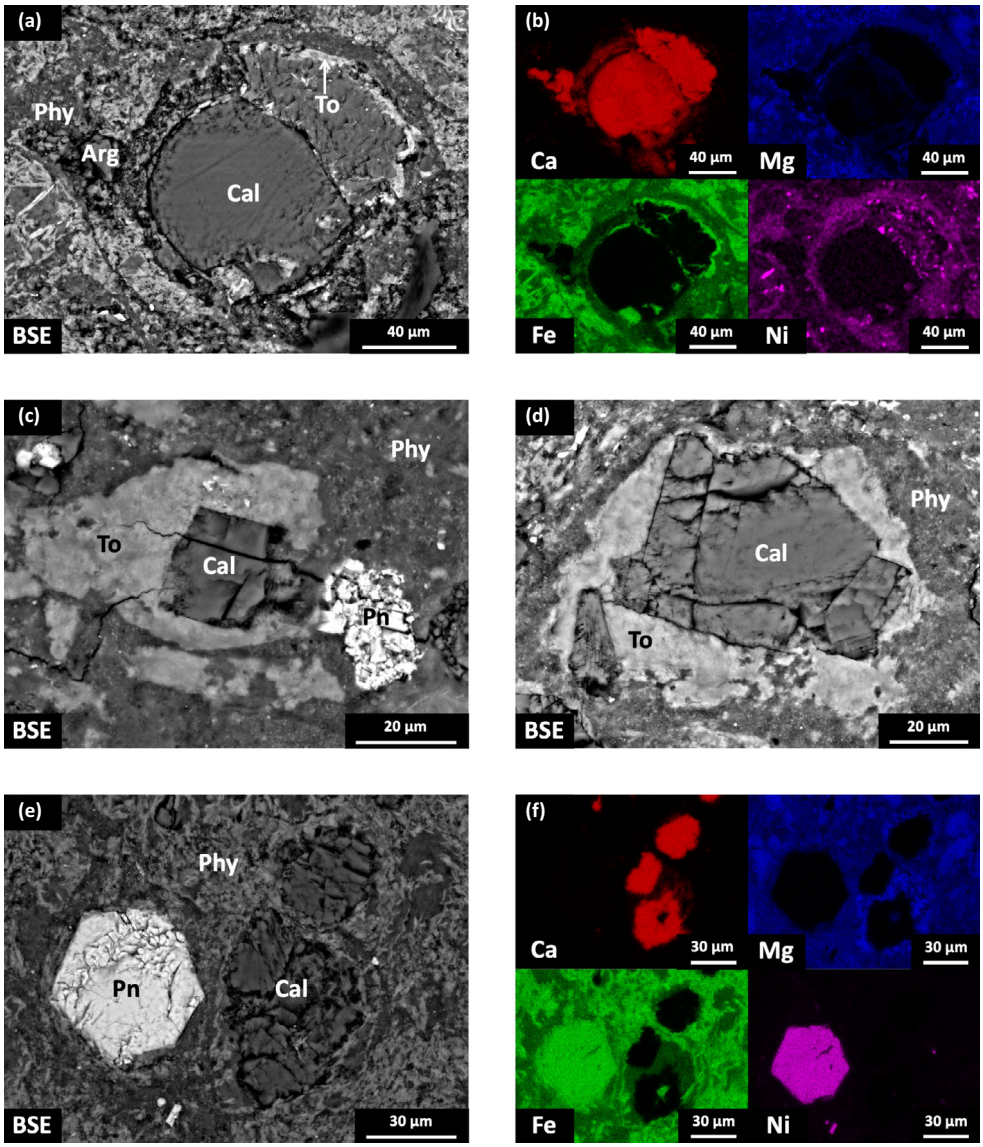

Fig. 2. a, b) BSE image and EDS element maps of assemblage 4 representing a chondrule pseudomorph: aragonite + calcite (Arg) and calcite (Cal) with tochilinite (To) rim embedded in phyllosilicate-rich (Phy) matrix. c) BSE images and EDS element maps of assemblage 5: calcite (Cal) with tochilinite (To) rim in association with pentlandite (Pn) embedded in phyllosilicate-rich (Phy) matrix. d) BSE image and EDS element maps of assemblage 6: calcite (Cal) with tochilinite (To) rim embedded in phyllosilicate-rich (Phy) matrix. e, f) BSE image and EDS element maps of assemblage 7: calcite (Cal) in association with pentlandite (Pn) embedded in phyllosilicate-rich (Phy) matrix.

calcite crystals. The large dolomite crystals show zoning visible in CL images (Figs. 3e and 3f). Dolomite has a Ca/Mg molar ratio ranging from to 0.9 to 1.1 and is rich in Mn and Fe (MnO: 3.41–5.18 wt%, FeO: 2.36–3.76 wt%, $n = 6$).

Assemblage 9 consists of octahedral magnetite crystals with interstitial calcite and phyllosilicate (Fig. 4). Magnetite is dispersed in some highly altered regions of Cold Bokkeveld matrix (Barber 1981). It may form by the alteration of pyrrhotite; magnetite crystals often pseudomorph pyrrhotite in carbonaceous chondrites (Zolensky et al. 2002; Gounelle and Zolensky 2014). Here, no obvious pseudomorphs were observed, but the lack of larger sulfide crystals in the magnetite-rich parts of the thin section further supports this interpretation.

Aside from carbonate minerals, other Ca-rich assemblages include calcium–aluminum-rich inclusions (CAIs) (Fig. 5). The numerous CAIs found in the studied thin section are predominantly spinel-pyroxene CAIs, the most abundant group of CAIs in Cold Bokkeveld (Greenwood et al. 1994). All observed CAIs

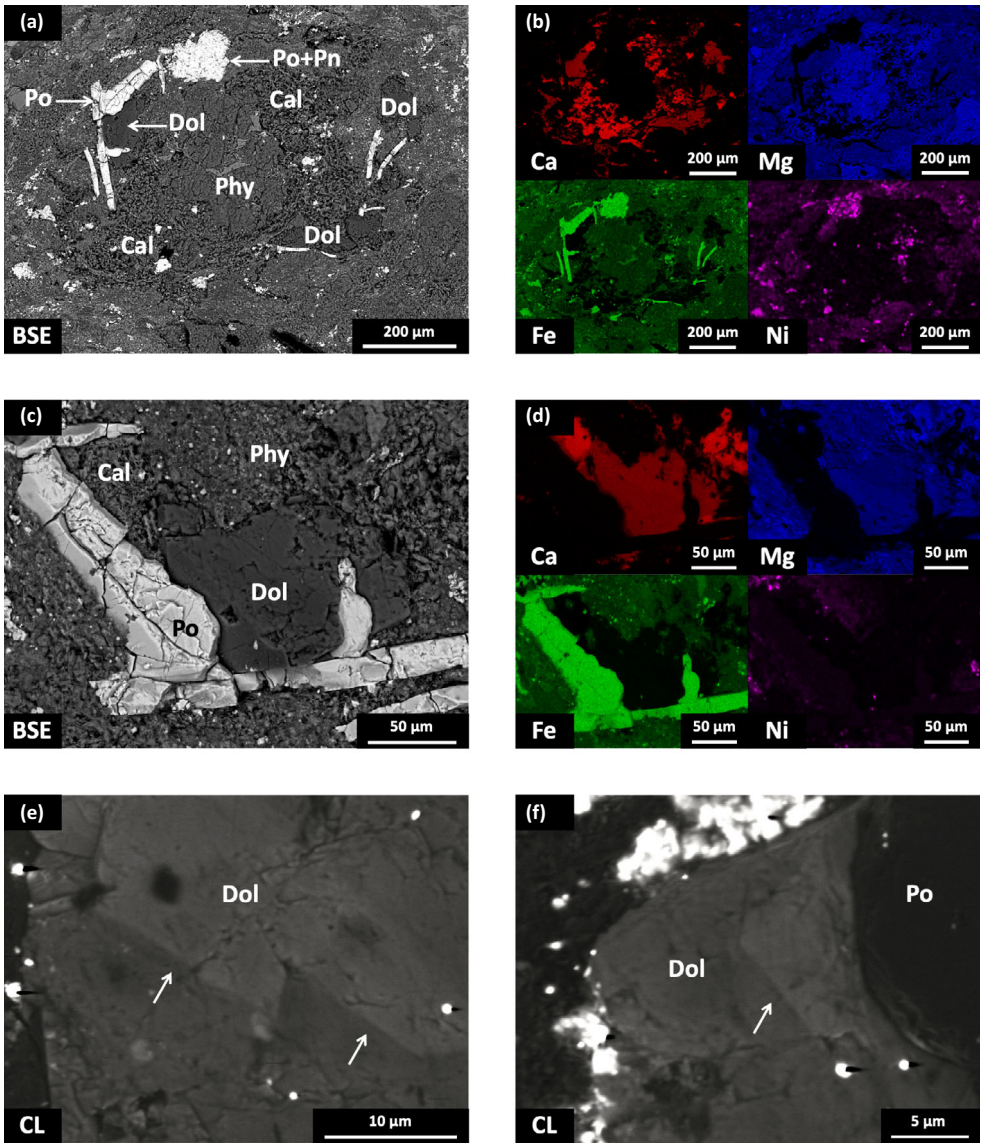

Fig. 3. a–d) BSE image and EDS element maps of assemblage 8 representing a chondrule pseudomorph: pyrrhotite (Po) and pentlandite (Pn) with interstitial dolomite (Dol), calcite (Cal), and phyllosilicate (Phy). Note that (c) and (d) are higher magnification areas of (a) and (b). e, f) CL images of part of assemblage 8: dolomite (Dol) shows zoning indicated by arrows.

have prominent Ca-rich pyroxene rims. They are spinel-dominated and often contain perovskite crystals. In one case, a corundum crystal and a perovskite crystal are found with interstitial spinel. Although calcium carbonate is reported to exist in 8% of the CAIs of Cold Bokkeveld (Greenwood et al. 1994), we have not been able to locate any in CAIs.

Raman Spectroscopy

Raman spectroscopy is a fast and robust method to distinguish between carbonate minerals and to detect organic carbon in the structures of carbonates. The latter results from the ability of calcite (and other carbonates) to adsorb organic matter onto their surfaces while they are growing (e.g., Suess 1970). A brief overview of Raman-active modes of carbonate minerals and organic carbon is provided in Appendix S1 in supporting information.

Raman spectra of carbonates in assemblages 1 and 2 could not be collected because of their sensitivity to the Raman laser. Even lowering the laser power to 1% of the power used for carbonates in the other assemblages caused instantaneous burning of the samples.

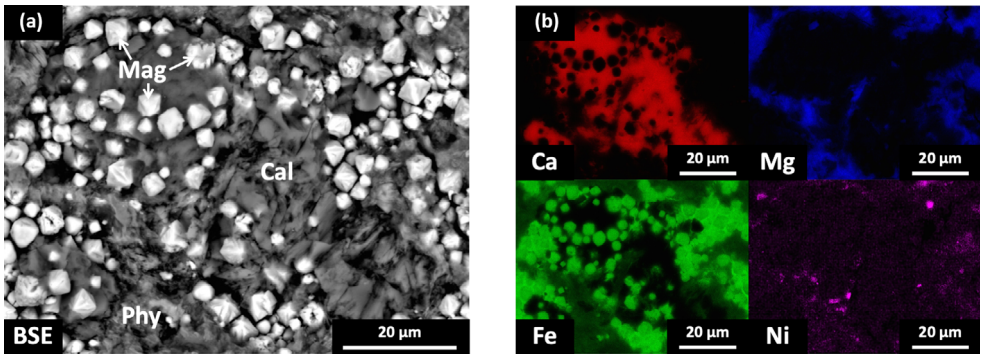

Fig. 4. BSE image and EDS element maps of assemblage 9: magnetite (Mag) with interstitial calcite (Cal) embedded in phyllosilicate-rich (Phy) matrix.

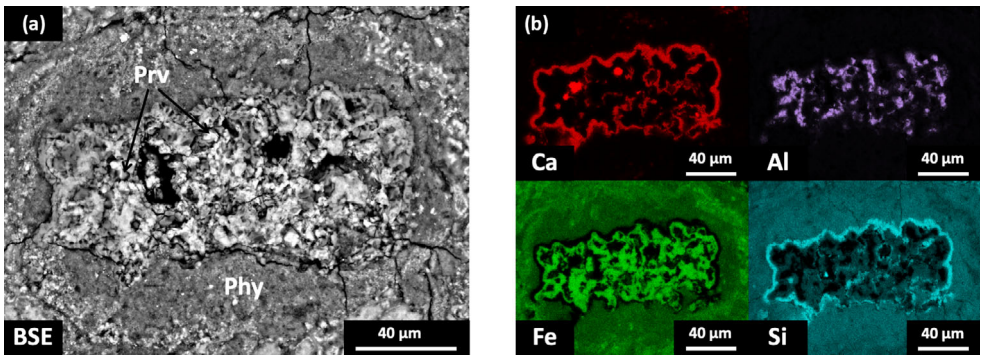

Fig. 5. BSE image and EDS element maps of a calcium-aluminum-rich inclusion with perovskite (Prv) embedded in phyllosilicate-rich (Phy) matrix.

Representative Raman spectra of carbonates from the other assemblages in Cold Bokkeveld as well as from terrestrial reference samples are presented in Fig. 6. The Raman spectrum of the $CaCO_3$ grain in assemblage 4, next to type 2 calcite grains, shows four broad peaks at 144, 172, 194, and 265 cm^{-1} (Fig. 6). Peaks at 172 and 194 cm^{-1} can be assigned to aragonite, while those at 144 and 265 cm^{-1} to calcite, indicating an aragonite-calcite phase mixture. Aragonite in contact with calcite in Cold Bokkeveld was described previously (Barber 1981). The spectrum of aragonite from assemblage 4 also contains broad, low-intensity G and D bands at 1390 and 1588 cm^{-1}, respectively, corresponding to organic carbon.

Spectra of calcite were collected from six of the assemblages (Table 3, Fig. 6). In order to compare the characteristics of Raman spectra of meteoritic and terrestrial calcite, spectra of nine calcites from several terrestrial geological settings were also collected. These include calcites precipitated from hydrothermal fluids in cavities within basalts from Bulhary and Hajnáčka, Slovakia; prismatic calcite collected from a cavity within an outcrop of serpentinized peridotite in a mélange in the Othris ophiolite, Greece; calcite representing bulk marble from Tuhár, Slovakia; calcite in a cavity of marble from Ružiná, Slovakia; calcites in limestone from Gemerská Ves and Margecany, Slovakia; calcite from a speleothem from the Peştera Şugău, Romania; and a large single crystal calcite from Dúhová priepasť cave, Slovakia. Despite having different origins and formation mechanisms, the frequencies of the six calcite peaks were relatively uniform, ranging 156–157, 281–282, 711–712, 1085, 1434–1435, and 1748–1750 cm^{-1}. In contrast, the peak positions of calcite from Cold Bokkeveld show significant variation (Figs. 7a–c). The range for external modes, involving bonds between Ca^{2+} cations and the CO_3^{2-} groups, exceeds 10 cm^{-1}. Of the analyzed meteoritic calcites, the peaks of type 2 calcite in assemblage 4 plot the closest to the terrestrial ones. Type 1 calcite grains have peak positions at significantly lower frequencies and calcite in assemblage 3 at even lower frequencies (Figs. 7a–c). The positions of Raman peaks corresponding to external modes (measured at 142 and 259 cm^{-1}) in calcite in assemblage 3 are lower than those of any (including exotic) naturally occurring terrestrial rhombohedral carbonate measured using the same instrumental

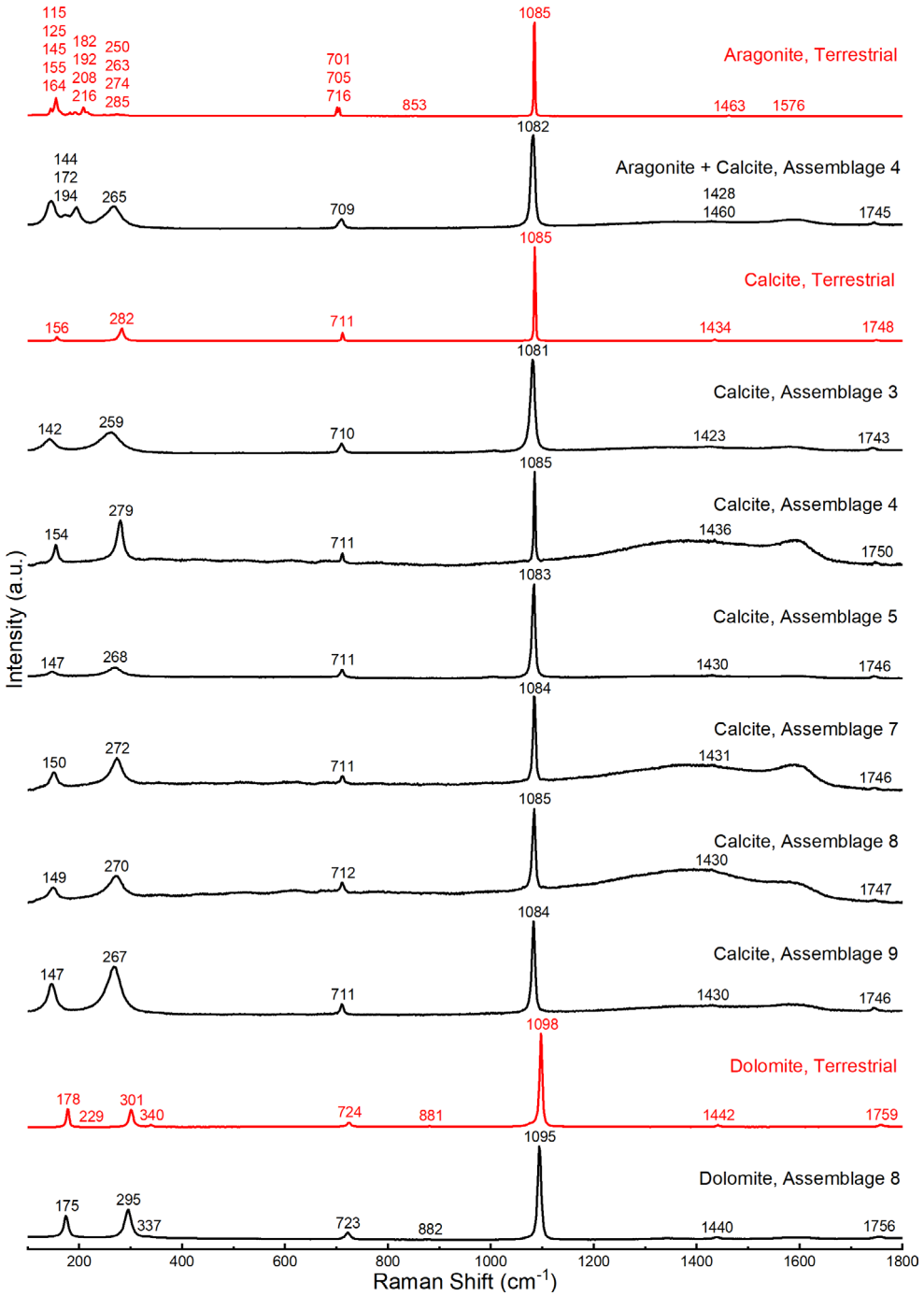

Fig. 6. Raman spectra of carbonates in Cold Bokkeveld CM chondrite. Peak positions corresponding to carbonate modes are marked. The wide bands around 1355 and 1575 cm^{-1} represent the D and G bands of carbon, respectively, and indicate the presence of organic material in the carbonates. Raman spectra of terrestrial aragonite, dolomite (Farsang et al. 2018), and calcite were taken at 25 °C.

conditions (Farsang et al. 2018, 2021). Raman spectra of most of the meteoritic calcites contain broad G and D bands, indicating the presence of organic carbon in their structure (Table 3). The intensity of these peaks relative to the highest intensity ν_1 carbonate peak and relative to each other varies greatly, suggesting large differences in organic carbon content and speciation (Fig. 6).

The meteoritic and terrestrial calcites also differ in the line widths of their Raman modes, with the full

Table 3. Peak positions and corresponding full width half maxima of the calcite and organic carbon bands.

Sample	Type	T	FWHM	L	FWHM	ν_4	ν_1	FWHM	ν_3	$2\nu_2$	D	G
Cold Bokkeveld												
Assemblage 3		142	24	259	47	710	1081	10	1423	1743	1383	1576
Assemblage 4	2a	154	9	279	14	711	1085	3	1436	1750	1398	1591
Assemblage 5	1a	147	18	268	32	711	1083	7	1430	1746	1399	1587
Assemblage 7	1b	150	18	272	26	711	1084	6	1431	1746	1401	1592
Assemblage 8	1a	149	21	270	33	712	1085	7	1430	1747	1383	1570
Assemblage 9	1c	147	18	267	34	711	1084	7	1430	1746	1403	1589
Terrestrial samples												
Bulhary		156	7	282	10	711	1085	3	1435	1750		
Dúhová priepasť		156	7	282	10	711	1085	3	1434	1750		
Gemerská Ves		156	7	282	10	711	1085	3	1435	1750		
Othris		156	8	282	11	711	1085	4	1434	1750		
Hajnáčka		157	11	282	13	712	1085	5	1435	1750		
Margecany		156	7	281	11	711	1085	3	1434	1750		
Ružiná		156	7	282	10	711	1085	3	1434	1750		
Peştera Şugău		157	9	282	13	712	1086	4	1436	1750		
Tuhár		156	8	282	11	712	1085	4	1435	1750		

All values are in cm^{-1}.

width half maximum (FWHM) of peaks broader in the Cold Bokkeveld assemblages than that in terrestrial carbonates by up to ~30 cm^{-1}. The only exception is type 2 calcite in assemblage 4 that shows comparable peak widths with terrestrial carbonates. We also note that for the two external modes and the highest intensity ν_1 internal mode, there is a strong negative correlation ($R^2 = 0.80$, 0.97, and 0.87, respectively) between the peak position and FWHM of the peak (Figs. 7d–f).

The Raman spectrum of dolomite in assemblage 8 exhibits all the peaks characteristic of dolomite except the lowest intensity 229 cm^{-1} peak. As for calcite, the peak positions of Cold Bokkeveld dolomite are lower (except the very low-intensity 882 cm^{-1} peak) and FWHM values higher than that of the terrestrial reference sample. The G and D bands indicative of organic carbon are broad and of low intensity, significantly lower than in calcite in the same assemblage.

Oxygen Isotopes

The presence of large dolomite grains in assemblage 8 with cavity and impurity-free regions allowed the measurement of ^{17}O and ^{18}O isotopes in this phase. The oxygen isotopic compositions of dolomite grains we have measured, as well as previous measurements conducted on dolomite grains in CM and C chondrites and other carbonate phases in Cold Bokkeveld, are reported in Table 4. While $\delta^{18}O$ values for dolomite reported here are very similar to those previously reported for Cold Bokkeveld (Benedix et al. 2003) and ALH 84049 (Tyra et al. 2016) CM chondrites, and the Sutter's Mill C chondrite (Jenniskens et al. 2012), the $\Delta^{17}O$ values are slightly lower. Compared to calcite, our dolomite $\delta^{18}O$ values are between those typical of type 1 and type 2 calcite that have average $\delta^{18}O$ of ~32–36 and 21–24‰, respectively (Lindgren et al. 2017), whereas $\Delta^{17}O$ values of dolomite are typically lower (Benedix et al. 2003; Lindgren et al. 2017), ranging from −4.9 to −4.0‰.

DISCUSSION

Crystallinity of Carbonates

The dark speckled appearance of carbonates in assemblage 1 and 2, in contrast to the bright appearance of other carbonates in reflected light, and their behavior in the laser beam suggest that these carbonates are microcrystalline and rich in opaque, probably organic material-rich particles that absorb optically and result in excessive heating from the Raman laser.

In assemblage 4, where a grain consisting of an aragonite/calcite phase mixture and crystals of type 2 calcite are also present, aragonite may be a primary phase and type 2 calcite a secondary replacement as suggested by Lee et al. (2014). If this is the case, the replacement does not involve the full dissolution of aragonite followed by the precipitation of calcite. Instead, the bimineralic grain may document a gradual aragonite-calcite phase transition. This phase transition has been observed experimentally at temperatures ranging from 385 to 468 °C (Antao and Hassan 2010;

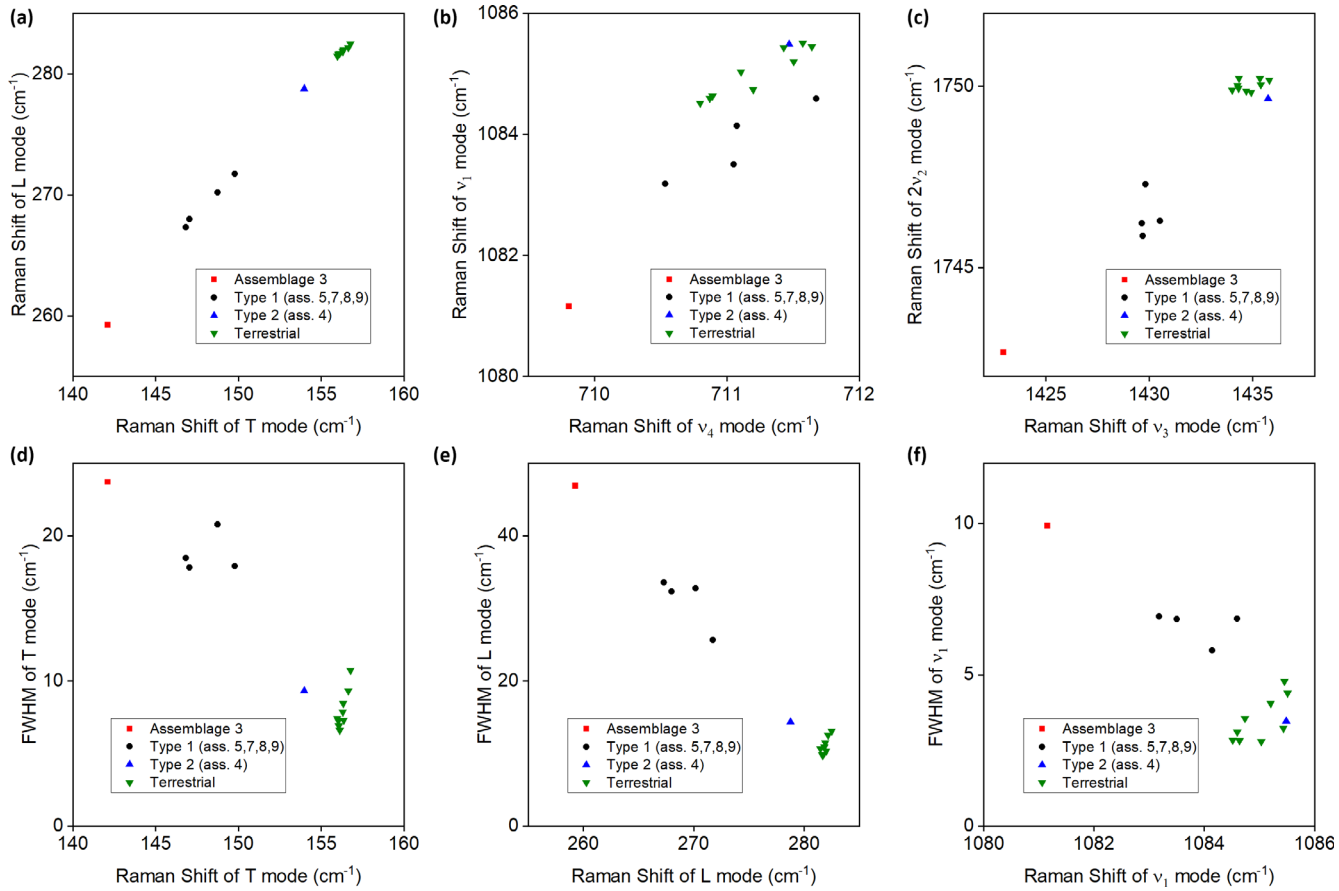

Fig. 7. a–c) Raman shifts in calcite in six different assemblages in Cold Bokkeveld CM chondrite and nine terrestrial samples. d–f) FWHM as a function of peak position of the external (translational, T and librational, L) modes and highest intensity ν_1 internal mode.

Parker et al. 2010; Farsang et al. 2018) and the Raman spectra collected upon the transition exhibit similar features to those seen here (Farsang et al. 2021). The transition is typically inhibited kinetically by the large associated volume change (from ~34 to ~37 cm^3 mol^{-1} as aragonite transforms to calcite), but the presence of aqueous fluids can significantly accelerate the kinetics and lower the effective activation energy for the phase transition, such that it may then occur at much lower temperatures (Bischoff and Fyfe 1968). In the presence of water, at 108 °C, the transition requires hours to days to take place, while at ambient temperatures it would require months to years (Bischoff and Fyfe 1968).

Partial substitution of smaller cations (e.g., Mg^{2+}) for Ca^{2+} is often responsible for an increase in frequency of Raman or infrared modes in calcite. For instance, the ν_1 peak positions of calcites in some CM2 chondrites have been found to be 2–3 cm^{-1} higher than in pure terrestrial calcites, a feature attributed to significant levels of cations other than Ca^{2+} (Chan et al. 2017). Generally, the smaller the cation, the shorter the interatomic distances, resulting in shifts to higher frequency (Krishnamurti 1956). In this study, though, we see the opposite effect, i.e., some chondritic calcite peaks appear shifted to significantly lower frequency positions (by ~1 to 20 cm^{-1} in calcite in assemblage 3) than in the pure, highly crystalline abiotic terrestrial calcites. It is not certain what causes the red shift of these peaks. Substitution of large cations (e.g., K^+) for Ca^{2+} could lead to the observed decrease in frequency, but chemical analysis showed no enrichment by an element that would have an ion bigger than Ca^{2+}. A large shift of peaks corresponding to external modes (>10 cm^{-1}) requires significant and measurable substitution. Previous work has shown that the peak positions in calcites with abundant organic material are very similar to those of organic-carbon-free calcites and differ by no more than ~1 cm^{-1} (Chan et al. 2017), so the presence of organic carbon cannot be invoked as a reasonable explanation either. Therefore, we speculate that the extreme shifts in peak positions of calcite in assemblage 3 may be explained by changes in local environment during the Raman spectroscopic analysis rather than compositional changes. We note that calcite

Table 4. Oxygen isotopic compositions of dolomite grains in CM and C chondrites and other carbonate phases in Cold Bokkeveld.

Meteorite	$\delta^{17}O$	$\delta^{18}O$	$\Delta^{17}O$	Type of measurement	*n*	Reference
Dolomite in CM chondrites						
Cold Bokkeveld	8.5 ± 1.6 (2σ)	25.8 ± 1.0 (2σ)	−4.9 ± 1.7 (2σ)	In situ		This work
	7.8 ± 1.6 (2σ)	23.9 ± 1.0 (2σ)	−4.6 ± 1.7 (2σ)	In situ		
	7.0 ± 1.6 (2σ)	21.1 ± 1.0 (2σ)	−4.0 ± 1.7 (2σ)	In situ		
Cold Bokkeveld	12	25.9	−1.51	Bulk sample		Benedix et al. (2003)
ALH 84049	From 10.3 ± 1.5 to 15.9 ± 1.6 (1σ)	From 25.4 ± 1.7 to 30.4 ± 1.6 (1σ)	From −3.1 ± 1.5 to 0.9 ± 1.6 (1σ)	In situ	11	Tyra et al. (2016)
ALH 84034*	From 3.1 ± 0.9 to 17.7 ± 1.1 (2σ)	From 8.6 ± 0.7 to 22.1 ± 3.1 (2σ)	From −1.6 ± 3.2 to 6.9 ± 1.2 (2σ)	In situ	6	Telus et al. (2019)
ALH 83100	From 8.7 ± 0.3 to 15.0 ± 0.9 (2σ)	From 20.1 ± 1.2 to 23.8 ± 0.8 (2σ)	From −2.6 ± 0.7 to 3.5 ± 1.5 (2σ)	In situ	11	Telus et al. (2019)
MET 01070	From 0.3 ± 0.2 to 12.4 ± 0.2 (2σ)	From 9.5 ± 0.7 to 22.2 ± 0.7 (2σ)	From −8.6 ± 1.3 to 2.3 ± 1.3 (2σ)	In situ	4	Telus et al. (2019)
Dolomite in C chondrites						
Sutter's Mill	From 8.8 ± 1.1 to 10.6 ± 1.1 (2σ)	From 23.5 ± 1.1 to 26.1 ± 1.2 (2σ)	From −4.0 ± 1.4 to −2.8 ± 1.3 (2σ)	In situ	11	Jenniskens et al. (2012)

Mineral phase	$\delta^{17}O$	$\delta^{18}O$	$\Delta^{17}O$	Type of measurement	*n*	Reference
Carbonate phases in Cold Bokkeveld						
Carbonate		26.6		Bulk sample		Grady et al. (1988)
		29.8		Bulk sample		
Calcite	13.1	28.3	−1.65	Bulk sample		Benedix et al. (2003)
Carbonate		From 28.2 ± 0.2 to 34.6 ± 0.2 (1σ)		Bulk sample	3	Guo and Eiler (2007)
Carbonate		30.4 ± 0.4		Bulk sample		Alexander et al. (2015)
Ca-carbonate	From 10.6 ± 0.7 to 15.7 ± 0.8 (2σ)	From 20.6 ± 1.0 to 28.2 ± 1.0 (2σ)	From −0.7 ± 0.5 to 1.7 ± 0.5 (2σ)	In situ	10	Verdier-Paoletti et al. (2017)
Type 1 calcite	From 12.1 ± 2.3 to 21.0 ± 1.9 (2σ)	From 30.8 ± 0.9 to 38.8 ± 1.7 (2σ)	From −4.5 ± 2.6 to 1.7 ± 2.2 (2σ)	In situ	9	Lindgren et al. (2017)
Type 2 calcite	From 2.5 ± 2.3 to 16.9 ± 2.3 (2σ)	From 11.9 ± 1.6 to 36.8 ± 1.2 (2σ)	From −3.7 ± 2.5 to −1.8 ± 2.2 (2σ)	In situ	4	Lindgren et al. (2017)

All values are in ‰.
All relative to standard mean ocean water (SMOW).
*The cited ranges refer to dolomite grains not containing calcite.

in assemblage 3 is almost entirely surrounded by pyrrhotite, pentlandite, and magnetite, i.e., phases that have much higher thermal conductivity than phyllosilicates, in which the other calcite grains occur. Consequently, the Raman laser may heat up the entire assemblage, resulting in lower measured frequency values (Farsang et al. 2018).

Peak widths of chondritic calcites are generally much larger than those of terrestrial carbonates. The only exception is type 2 calcite in assemblage 4, implying high crystallinity for type 2 calcite. Broadened peaks generally indicate either inhomogeneous and extensive substitution by a cation of a different size or an increase in local strain, possibly related to lower crystallinity, smaller effective correlated structure, and the abundance of structural defects.

The lower peak positions and higher FWHM values in Cold Bokkeveld dolomite than that in the terrestrial reference sample also indicate the presence of impurities and/or lower crystallinity, consistent with significant Mn- and Fe-enrichment.

Carbonate Formation Conditions

Oxygen isotopes in carbonate minerals can be used to infer the properties of the aqueous fluid from which they originated, the temperatures at which they formed, and the degree of aqueous alteration on the CM parent body (Johnson and Prinz 1993; Riciputi et al. 1994; Benedix et al. 2003; Guo and Eiler 2007; Lee et al. 2013, 2014; Lindgren et al. 2017; Verdier-Paoletti et al. 2017; Telus et al. 2019). In the presence of aqueous

fluid, significant oxygen isotope diffusional exchange between the fluid and calcite (and other carbonates) occurs at moderate temperatures of 400–500 °C (Farver 1994). Since these temperatures were probably not reached in the CM parent body(ies) (see below), the oxygen isotopic composition of the carbonates is related to that of the original fluid and has not been subject to subsequent re-equilibration and can therefore provide valuable information on the evolution and chemistry of the fluid from which the carbonates precipitated. Variations in O isotopic composition between carbonate grains can imply different formation temperatures, sources of fluid, or evolving fluid composition for CM chondrites (Chan et al. 2017).

Our measurements reveal that dolomite has $\delta^{18}O$ values intermediate between those of type 1 and type 2 calcite, supporting the idea of dolomite precipitation occurring between the main stages of type 1 and type 2 calcite formation (Lindgren et al. 2017). However, it should be pointed out that the O isotopic values of type 1 and type 2 calcite and dolomite may overlap with one another (Fig. 8) and it is possible that any of these phases form from fluids of very similar composition. Indeed, similar $\Delta^{17}O$ values measured in calcite and dolomite were previously invoked to imply that these two phases precipitated from the same fluid on CM parent bodies (Benedix et al. 2003). However, our dolomite $\Delta^{17}O$ values are typically lower than those measured in calcite with comparable $\delta^{18}O$ (Fig. 8a) (Benedix et al. 2003; Lindgren et al. 2017), suggesting precipitation from two fluids. Furthermore, the contact of calcite and dolomite in single carbonate grains in assemblage 8 (Fig. 3), with Fe/Ca and Mn/Ca ratios systematically higher in dolomite than coexisting calcite, point toward disequilibrium between these phases and distinct precipitation events (Riciputi et al. 1994). Based on the model prediction for the variation in carbonate isotopic composition as a function of formation temperature of Alexander et al. (2015), our measured $\delta^{18}O$ values suggest dolomite precipitation temperatures of ~70–100 °C. Given the lack of $\delta^{13}C$ data, these temperatures should be treated as first approximation. The activation of fluids and subsequent dolomite precipitation in CM chondrites was suggested to form in response to a transient heating event and/or a brief increase in fluid Mg/Ca ratios (Lindgren et al. 2017). Weight% levels of Mn in carbonates observed in this study and by Riciputi et al. (1994) suggest that dolomite concentrates this element.

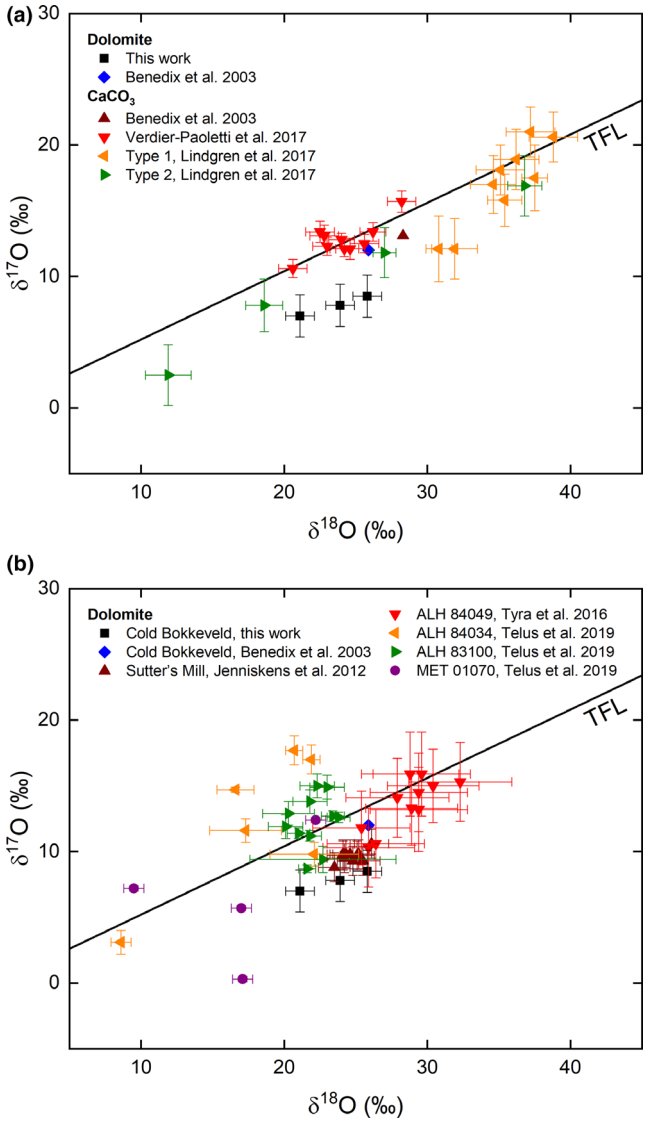

Fig. 8. Three isotope plots of (a) carbonate grains in Cold Bokkeveld and (b) dolomite grains in CM and C chondrites. Errors are 2σ. The solid line in each plot is the terrestrial fractionation line, defined as $\delta^{17}O = 0.52 \times \delta^{18}O$.

Paragenetic Sequence of the CM Chondrite Parent Body(ies)

The CM chondrite parent body(ies) underwent extensive aqueous alteration as shown by the presence of secondary minerals (e.g., McSween 1979; Brearley [2006] and references therein). The diversity and distribution of lithic clasts and mineral fragments showing various degrees of aqueous alteration (Bischoff et al. 2017; Lentfort et al. 2020) indicate that some alteration may have already taken place on precursor planetesimals, shortly before and/or while they accreted to their parent body(ies). Alternatively, lithic clasts and mineral fragments showing various degrees of aqueous alteration could be assembled from pieces of the same accreted parent body, although it is difficult to envisage a parent body brecciation process responsible for such a fine-scale distribution of these clasts and fragments. It is therefore possible that different lithic clasts and mineral

fragments record different aqueous alteration events (e.g., triggered by impacts), which either did not take place on the parent body or operated only locally on the parent body. In our reconstruction of the paragenetic sequence, we assume that much of the aqueous alteration happened on the finally accreted parent body, while recognizing that alternative scenarios may be possible.

During aqueous alteration, mesostasis was replaced by serpentine group minerals (Richardson 1981). Depending on the composition of the fluid and adjacent phases (e.g., S and Si activity), Fe,Ni-metal altered to tochilinite ($6Fe_{0.9}S{\cdot}5[Mg,Fe][OH]_2$), the Fe-rich phyllosilicate cronstedtite ($Fe^{2+}{}_2Fe^{3+}[SiFe^{3+}]O_5[OH]_4$) (with Fe,Ni-sulfide inclusions), magnetite, and accessory phases (Tomeoka et al. 1989; Hanowski and Brearley 2000; Brearley 2006; Palmer and Lauretta 2011). It has been proposed that the formation conditions for tochilinite correspond to temperatures at or below 170 °C and at pH 10–12 (Zolensky 1984). Most of the main primary sulfide in CM chondrites, troilite, was aqueously altered to secondary sulfides: pyrrhotite ($Fe_{[1-x]}S$ [$x = 0$–0.17] and pentlandite ($(Fe,Ni)_9S_8$; Brearley 2006). Iron-rich (fayalitic) olivine altered to Fe-rich phyllosilicates, followed by the alteration of Mg-rich (forsteritic) olivine to Mg-rich phyllosilicates and the alteration of pyroxene to phyllosilicates (Tomeoka et al. 1989; Brearley 2006). Extensive alteration of the CM chondrite parent body(ies) is also evident based on the presence of dolomite and complex carbonate grains with a $CaCO_3$ core and Mg-enriched rim (Fig. 3) (Zolensky et al. 1997).

The first carbonate minerals crystallized early on the CM chondrite parent body; e.g., ^{53}Mn–^{53}Cr radiometric dating of carbonates from four different CM chondrites yielded a formation age range of 4563.4+0.4/–0.5 Ma (Fujiya et al. 2012). The different stages of carbonate and serpentine formation almost certainly overlapped. Evidence was found in this study for calcite predating serpentine (and tochilinite) formation (see below), as also seen in other studies (Lee et al. 2013; Marrocchi et al. 2014; Fujiya et al. 2015; Verdier-Paoletti et al. 2017) and postdating the surrounding phyllosilicates (Barber 1981). These observations can be explained by the work of Lee et al. (2014), who suggest that carbonates in the CM2.5-CM2.2 chondrites experienced four distinct stages of mineralization including (1) the formation of aragonite, calcite, and dolomite by cementation of pore space; (2) the formation of tochilinite and Fe-rich serpentine replacing the edges of pore-filling carbonates; (3) the formation of Mg-rich serpentine replacing pore-filling carbonates; and finally, (4) calcite replacing dolomite and remaining anhydrous silicates (Lee et al. 2014). Observations of aragonite apparently being replaced by calcite (Fig. 2a) and tochilinite attacking calcite grains (Figs. 1c, 1d, 2c, and 2d) support this model. However, based on our petrographic observations, we propose two additional mineral forming events. In assemblage 9, octahedral magnetite crystals likely replace sulfide minerals (Fig. 4). The lack of S-bearing alteration products (e.g., tochilinite) in the vicinity of thousands of magnetite crystals indicates that, at least locally, the formation of interstitial calcite postdates the sulfur mobilization (and S-bearing secondary mineral formation) event. This is in contrast with type 1a or 1b calcite precipitating prior to tochilinite formation. We therefore propose a new type of calcite, type 1c. Furthermore, the fine-grained tochilinite rim indicates that at least one additional sulfur mobilization/tochilinite formation event occurred even after type 2 calcite formation (Fig. 2a). A high-temperature event, such as an impact, could have provided the heat necessary not only for late-stage calcite precipitation, resulting in type 2 calcite (Tyra et al. 2012), but also to initiate the spectroscopically documented aragonite-calcite phase transition also enhanced by the presence of aqueous fluids (Fig. 6). Isotopic measurements indicate that carbonates on the Cold Bokkeveld parent body formed roughly at the same time or equilibrated at the same temperature as serpentines (Verdier-Paoletti et al. 2017). Based on our observations, we propose at least six stages of potentially overlapping carbonate and phyllosilicate formation events (Fig. 9).

Carbonates in assemblages 1, 2, and 3 do not show the characteristics typical of type 1 or type 2 carbonates. Those in assemblages 1 and 2 are interstitial to pentlandite and share unusual optical features (Figs. 1a and 1c). The complex nature of carbonate in assemblage 1 (a $CaCO_3$ core with an Mg-enriched rim) and tochilinite replacing calcite in assemblage 2 indicate that this kind of carbonates formed at the very early stages of aqueous activity on the CM parent body. There are two possible formation scenarios for the carbonate grain in assemblage 1 (Figs. 1a and 1b): either it was originally calcic and exchanged cations with Mg-rich fluid or it precipitated from a fluid that changed from being Ca to Mg rich. Complex carbonates with Ca-carbonate–dominated cores have been observed before in the QUE 93005 CM2 chondrite and, regardless of which of the two formation scenarios outlined operated, indicate that the Ca-carbonates formed earlier (Rubin et al. 2007). In assemblage 3, part of the pyrrhotite grain with pentlandite rim clearly dissolved (Figs. 1e and 1f). The lack of S-bearing alteration products (such as tochilinite) in its vicinity indicates that the dissolution of sulfide and the

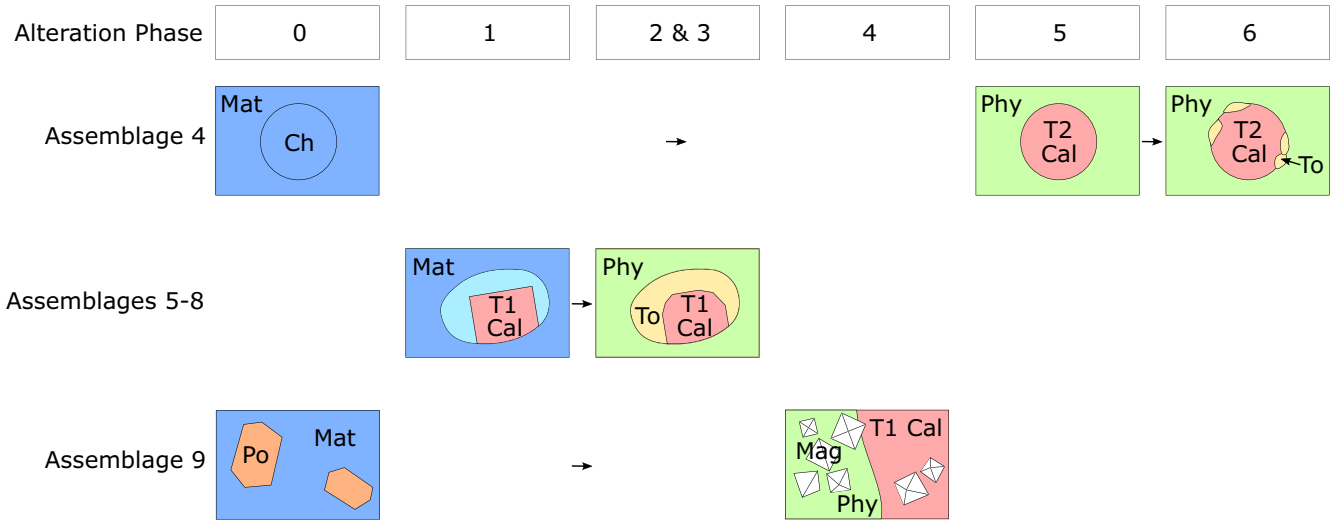

Fig. 9. Phases of aqueous alteration in Cold Bokkeveld reconstructed from petrographic features in carbonate assemblages 4–9 and based on Lee et al. (2014). Phase 0 represents the unaltered starting material with chondrules (Ch) and sulfides (e.g., pyrrhotite, Po) embedded in silicate-dominated matrix (Mat). In phase 1, aragonite, type 1 calcite (T1 Cal) and dolomite grow; phases 2 and 3 are dominated by phyllosilicate (Phy) and tochilinite (To) formation; in phase 4 type 1c calcite interstitial to magnetite (Mag) precipitates; in phase 5 type two calcite (T2 Cal) grows; and phase 6 represents another tochilinite formation event.

precipitation of the spectroscopically distinct calcite also took place very early on the CM parent body.

The presence of organic carbon in most of the analyzed carbonate grains (Fig. 6) indicates that organic carbon was mobilized by aqueous fluids for extended periods. For comparison, disordered organics were present in only ~25% of analyzed CM chondritic carbonate grains (Chan et al. 2017). The large variability in G and D band positions (Table 3) suggests that organic carbon modified by distinct heating processes has been incorporated into the carbonate minerals (Quirico et al. 2018).

The diverse compositions and petrographic features of carbonates and associated phases indicate precipitation from locally formed, physically restricted aqueous fluids that only penetrated through small regions. This interpretation is consistent with highly variable O isotopic compositions in carbonates (e.g., Telus et al. 2019). Different fluid compositions, in turn, may arise from the heterogeneity of accreted ices and mineral assemblages in Cold Bokkeveld clasts that range from CM2.7 to CM2.1 (Bischoff et al. 2017; Lentfort et al. 2020). The intrasample mineralogical heterogeneity in different CM chondrites, including Cold Bokkeveld, reflects either sampling from different source regions within the CM parent body(ies) or from different precursor planetesimals, possibly following their early-stage fracturing in the protoplanetary disk. Impacts and collisions with water- or ice-rich bodies (or water- or ice-rich dust clouds) could have led to the introduction of water and/or heating events on the CM parent body(ies), followed by alteration and mineral forming events that only a subset of CM chondrites exhibit.

CONCLUSIONS

Our study reveals the existence of carbonates that display petrographic features quite distinct from those of type 1 and type 2 carbonates. These include carbonates interstitial to octahedral magnetite crystals, for which a new designation of "type 1c" is suggested. Abundant dolomite with high Mn contents has been found. The O isotopic values of dolomite ($\delta^{18}O$ ranging from 21.1 to 25.8‰ and $\Delta^{17}O$ from −4.9 to −4.0‰) are similar to those measured in dolomites from other CM chondrites. The presence of complex carbonates with a $CaCO_3$ core and Mg-enriched rim implies several generations of fluids and/or their evolving composition on the CM parent body(ies). Petrographic characteristics indicate at least six stages of potentially overlapping carbonate and phyllosilicate formation events, probably enhanced by heat generated due to collisional events. We show that type 1 and type 2 calcite have distinct spectral characteristics (peak positions and widths) and can be distinguished using Raman spectroscopy. Type 1 calcite displays very broad Raman peaks, whereas type 2 calcite yields Raman spectra with very narrow peak widths, similar to those of terrestrial calcite, suggesting very high crystallinity. We report Raman spectral evidence for an aragonite-calcite phase transition. Raman spectroscopy also revealed the presence of organic matter in the majority

of carbonates. This indicates that organic carbon was mobilized by aqueous fluids for extended periods.

Acknowledgments—We thank Caroline Smith and Natasha Almeida of the Natural History Museum, London for the loan of thin section Cold Bokkeveld P5449 from BM.1727; Iris Buisman and Giulio I. Lampronti for their assistance with SEM and EPMA analysis; as well as Martin Lee, an anonymous reviewer, and the associate editor Mike Zolensky for their helpful comments and suggestions. This work was supported by the Royal Astronomical Society (Paneth Meteorite Trust Award to MMG), the Natural Environment Research Council (grant number NE/L002507/1), and the Science and Technology Facilities Council (grant number ST/P000657/1 for IAF at the Open University).

Editorial Handling—Dr. Michael Zolensky

REFERENCES

Alexander C. M. O'D., Bowden R., Fogel M. L., and Howard K. T. 2015. Carbonate abundances and isotopic compositions in chondrites. *Meteoritics & Planetary Science* 50:810–833.

Antao S. M. and Hassan I. 2010. Temperature dependence of the structural parameters in the transformation of aragonite to calcite, as determined from in situ synchrotron powder X-ray-diffraction data. *The Canadian Mineralogist* 48:1225–1236.

Barber D. J. 1981. Matrix phyllosilicates and associated minerals in C2M carbonaceous chondrites. *Geochimica et Cosmochimica Acta* 45:945–970.

Beck P., Quirico E., Montes-Hernandez G., Bonal L., Bollard J., Orthous-Daunay F.-R., Howard K. T., Schmitt B., Brissaud O., Deschamps F., Wunder B., and Guillot S. 2010. Hydrous mineralogy of CM and CI chondrites from infrared spectroscopy and their relationship with low albedo asteroids. *Geochimica et Cosmochimica Acta* 74:4881–4892.

Benedix G. K., Leshin L. A., Farquhar J., Jackson T. L., and Thiemens M. H. 2003. Carbonates in CM2 chondrites: Constraints on alteration conditions from oxygen isotopic compositions and petrographic observations. *Geochimica et Cosmochimica Acta* 67:1577–1588.

Bischoff A. 1998. Aqueous alteration of carbonaceous chondrites: Evidence for preaccretionary alteration—A review. *Meteoritics & Planetary Science* 33:1113–1122.

Bischoff A., Ebert S., Metzler K., and Lentfort S. 2017. Breccia classification of CM chondrites (abstract). 80th Annual Meeting of the Meteoritical Society. Meteoritics & Planetary Science 52.

Bischoff J. L. and Fyfe W. S. 1968. Catalysis, inhibition, and the calcite-aragonite problem; [Part] 1, The aragonite-calcite transformation. *American Journal of Science* 266:65–79.

Brearley A. J. 2006. The action of water. In *Meteorites and the early solar system II*, edited by Lauretta D. S. and Mcsween H. Y. Tucson, Arizona: The University of Arizona Press. pp. 587–624.

Brearley A. J. and Hutcheon I. D. 2002. Carbonates in the Y-791198 CM2 chondrite: Zoning and Mn-Cr systematic (abstract). *Meteoritics & Planetary Science* 37:A23.

Brearley A. J., Saxton J. M., Lyon I. C., and Turner G. 1999. Carbonates in the Murchison CM chondrite: CL characteristics and oxygen isotopic compositions (abstract #1301). 30th Lunar and Planetary Science Conference. CD-ROM.

Chan Q. H. S., Zolensky M. E., Bodnar R. J., Farley C., and Cheung J. C. H. 2017. Investigation of organo-carbonate associations in carbonaceous chondrites by Raman spectroscopy. *Geochimica et Cosmochimica Acta* 201:392–409.

de Leuw S., Rubin A. E., and Wasson J. T. 2010. Carbonates in CM chondrites: Complex formational histories and comparison to carbonates in CI chondrites. *Meteoritics & Planetary Science* 45:513–530.

Farsang S., Facq S., and Redfern S. A. T. 2018. Raman modes of carbonate minerals as pressure and temperature gauges up to 6 GPa and 500 °C. *American Mineralogist* 103:1988–1998.

Farsang S., Widmer R. N., and Redfern S. A. T. 2021. High-pressure and high-temperature vibrational properties and anharmonicity of carbonate minerals up to 6 GPa and 500 °C by Raman spectroscopy. *American Mineralogist* 106:581–598.

Farver J. R. 1994. Oxygen self-diffusion in calcite: Dependence on temperature and water fugacity. *Earth and Planetary Science Letters* 121:575–587.

Fujiya W., Sugiura N., Hotta H., Ichimura K., and Sano Y. 2012. Evidence for the late formation of hydrous asteroids from young meteoritic carbonates. *Nature Communications* 3:627.

Fujiya W., Sugiura N., Marrocchi Y., Takahata N., Hoppe P., Shirai K., Yuji S., and Hiyagon H. 2015. Comprehensive study of carbon and oxygen isotopic compositions, trace element abundances, and cathodoluminescence intensities of calcite in the Murchison CM chondrite. *Geochimica et Cosmochimica Acta* 161:101–117.

Gounelle M. and Zolensky M. E. 2014. The Orgueil meteorite: 150 years of history. *Meteoritics & Planetary Science* 49:1769–1794.

Grady M. M., Wright I. P., Swart P. K., and Pillinger C. T. 1988. The carbon and oxygen isotopic composition of meteoritic carbonates. *Geochimica et Cosmochimica Acta* 52:2855–2866.

Greenwood R. C., Lee M. R., Hutchison R., and Barber D. J. 1994. Formation and alteration of CAIs in Cold Bokkeveld (CM2). *Geochimica et Cosmochimica Acta* 58:1913–1935.

Guo W. and Eiler J. M. 2007. Temperatures of aqueous alteration and evidence for methane generation on the parent bodies of the CM chondrites. *Geochimica et Cosmochimica Acta* 71:5565–5575.

Hanowski N. P. and Brearley A. J. 2000. Iron-rich aureoles in the CM carbonaceous chondrites Murray, Murchison, and Allan Hills 81002: Evidence for in situ aqueous alteration. *Meteoritics & Planetary Science* 35:1291–1308.

Howard K. T., Benedix G. K., Bland P. A., and Cressey G. 2009. Modal mineralogy of CM2 chondrites by X-ray diffraction (PSD-XRD). Part 1: Total phyllosilicate

abundance and the degree of aqueous alteration. *Geochimica et Cosmochimica Acta* 73:4576–4589.

Howard K. T., Benedix G. K., Bland P. A., and Cressey G. 2011. Modal mineralogy of CM chondrites by X-ray diffraction (PSD-XRD): Part 2. Degree, nature and settings of aqueous alteration. *Geochimica et Cosmochimica Acta* 75:2735–2751.

Jenniskens P., Fries M. D., Yin Q.-Z., Zolensky M., Krot A. N., Sandford S. A., Sears D., Beauford R., Ebel D. S., Friedrich J. M., Nagashima K., Wimpenny J., Yamakawa A., Nishiizumi K., Hamajima Y., Caffee M. W., Welten K. C., Laubenstein M., Davis A. M., Simon S. B. H., Philipp R., Young E. D., Kohl I. E., Thiemens M. H., Nunn M. H., Mikouchi T., Hagiya K., Ohsumi K., Cahill T. A., Lawton J. A., Barnes D., Steele A., Rochette P., Verosub K. L., Gattacceca J., Cooper G., Glavin D. P., Burton A. S., Dworkin J. P., Elsila J. E., Pizzarello S., Ogliore R., Schmitt-Kopplin P., Harir M., Grady M., Nagao K., Okazaki R., Takechi H., Hiroi T., Smith K., Silber E. A., Brown P. G., Albers J., Klotz D., Hankey M., Matson R., Fries J. A., Walker R. J., Puchtel I., Lee C.-T., Erdman M. E., Eppich G. R., Roeske S., Gabelica Z., Lerche M., Nuevo M., Girten B., and Worden S. P. 2012. Radar-enabled recovery of the Sutter's Mill meteorite, a carbonaceous chondrite regolith breccia. *Science* 338:1583–1588.

Johnson C. A. and Prinz M. 1993. Carbonate compositions in CM and CI chondrites and implications for aqueous alteration. *Geochimica et Cosmochimica Acta* 57:2843–2852.

Krishnamurti D. 1956. Raman spectrum of magnesite. *Proceedings of the Indian Academy of Sciences Section A* 43:210–212.

Lee M. R. 1993. The petrography, mineralogy and origins of calcium sulphate within the Cold Bokkeveld CM carbonaceous chondrite. *Meteoritics* 28:53–62.

Lee M. R., Sofe M. R., Lindgren P., Starkey N. A., and Franchi I. A. 2013. The oxygen isotope evolution of parent body aqueous solutions as recorded by multiple carbonate generations in the Lonewolf Nunataks 94101 CM2 carbonaceous chondrite. *Geochimica et Cosmochimica Acta* 121:452–466.

Lee M. R., Lindgren P., and Sofe M. R. 2014. Aragonite, breunnerite, calcite and dolomite in the CM carbonaceous chondrites: High fidelity recorders of progressive parent body aqueous alteration. *Geochimica et Cosmochimica Acta* 144:126–156.

Lentfort S., Bischoff A., Ebert S., and Patzek M. 2020. Classification of CM chondrite breccias—Implications for the evaluation of samples from the OSIRIS-REx and Hayabusa 2 missions. *Meteoritics & Planetary Science* 56:127–147.

Lindgren P., Lee M. R., Sofe M., and Burchell M. J. 2011. Microstructure of calcite in the CM2 carbonaceous chondrite LON 94101: Implications for deformation history during and/or after aqueous alteration. *Earth and Planetary Science Letters* 306:289–298.

Lindgren P., Lee M. R., Starkey N. A., and Franchi I. A. 2017. Fluid evolution in CM carbonaceous chondrites tracked through the oxygen isotopic compositions of carbonates. *Geochimica et Cosmochimica Acta* 204:240–251.

Marrocchi Y., Gounelle M., Blanchard I., Caste F., and Kearsley A. T. 2014. The Paris CM chondrite: Secondary minerals and asteroidal processing. *Meteoritics & Planetary Science* 49:1232–1249.

McSween H. Y. 1979. Are carbonaceous chondrites primitive or processed? A review. *Reviews of Geophysics and Space Physics* 17:1059–1078.

Palmer E. E. and Lauretta D. S. 2011. Aqueous alteration of kamacite in CM chondrites. *Meteoritics & Planetary Science* 46:1587–1607.

Parker J. E., Thompson S. P., Lennie A. R., Potter J., and Tang C. C. 2010. A study of the aragonite-calcite transformation using Raman spectroscopy, synchrotron powder diffraction and scanning electron microscopy. *CrystEngComm* 12:1590–1599.

Quirico E., Bonal L., Beck P., Alexander C. M. O'D., Yabuta H., Nakamura T., Nakato A., Flandinet L., Montagnac G., Schmitt-Kopplin P., and Herd C. D. K. 2018. Prevalence and nature of heating processes in CM and C2-ungrouped chondrites as revealed by insoluble organic matter. *Geochimica et Cosmochimica Acta* 241:17–37.

Richardson S. M. 1981. Alteration of mesostasis in chondrules and aggregates from three C2 carbonaceous chondrites. *Earth and Planetary Science Letters* 52:67–75.

Riciputi L. R., McSween H. Y., Johnson C. A., and Prinz M. 1994. Minor and trace element concentrations in carbonates of carbonaceous chondrites, and implications for the compositions of coexisting fluids. *Geochimica et Cosmochimica Acta* 58:1343–1351.

Rubin A. E., Trigo-Rodríguez J. M., Huber H., and Wasson J. T. 2007. Progressive aqueous alteration of CM carbonaceous chondrites. *Geochimica et Cosmochimica Acta* 71:2361–2382.

Saloman E. B. and Sansonetti C. J. 2004. Wavelengths, energy level classifications, and energy levels for the spectrum of neutral neon. *Journal of Physical and Chemical Reference Data* 33:1113–1158.

Śliwiński M. G., Kitajima K., Kozdon R., Spicuzza M. J., Fournelle J. H., Denny A., and Valley J. W. 2016. Secondary ion mass spectrometry bias on isotope ratios in dolomite-ankerite, Part I: $\delta^{18}O$ matrix effects. *Geostandards and Geoanalytical Research* 40:157–172.

Suess E. 1970. Interaction of organic compounds with calcium carbonate—I. Association phenomena and geochemical implications. *Geochimica et Cosmochimica Acta* 34:157–168.

Telus M., Alexander C. M. O'D., Hauri E. H., and Wang J. 2019. Calcite and dolomite formation in the CM parent body: Insight from in situ C and O isotope analyses. *Geochimica et Cosmochimica Acta* 260:275–291.

Tomeoka K., Mcsween H. Y., and Buseck P. R. 1989. Mineralogical alteration of CM carbonaceous chondrites: A review. *Proceedings of the NIPR Symposium on Antarctic Meteorites* 2:221–234.

Tomkinson T. O. R. 2013. *Constraining the formation conditions of the ancient Martian ALH 84001 carbonates*. Milton, UK: The Open University.

Tyra M., Brearley A., and Guan Y. 2016. Episodic carbonate precipitation in the CM chondrite ALH 84049: An ion microprobe analysis of O and C isotopes. *Geochimica et Cosmochimica Acta* 175:195–207.

Tyra M. A., Farquhar J., Wing B. A., Benedix G. K., Jull A. J. T., Jackson T., and Thiemens M. H. 2007. Terrestrial alteration of carbonate in a suite of Antarctic CM chondrites: Evidence from oxygen and carbon isotopes. *Geochimica et Cosmochimica Acta* 71:782–795.

Tyra M. A., Farquhar J., Guan Y., and Leshin L. A. 2012. An oxygen isotope dichotomy in CM2 chondritic carbonates—A SIMS approach. *Geochimica et Cosmochimica Acta* 77:383–395.

Verdier-Paoletti M. J., Marrocchi Y., Avice G., Roskosz M., Gurenko A., and Gounelle M. 2017. Oxygen isotope constraints on the alteration temperatures of CM chondrites. *Earth and Planetary Science Letters* 458:273–281.

Zolensky M. E. 1984. Hydrothermal alteration of CM carbonaceous chondrites: Implications of the identification of tochilinite as one type of meteoritic PCP. *Meteoritics* 19:346–347.

Zolensky M. E., Mittlefehldt D. W., Lipschutz M. E., Wang M.-S., Clayton R. N., Mayeda T. K., Grady M. M., Pillinger C., and Barber D. 1997. CM chondrites exhibit the complete petrologic range from type 2 to 1. *Geochimica et Cosmochimica Acta* 61:5099–5115.

Zolensky M. E., Nakamura K., Gounelle M., Mikouchi T., Kasama T., Tachikawa O., and Tonui E. 2002. Mineralogy of Tagish Lake: An ungrouped type 2 carbonaceous chondrite. *Meteoritics & Planetary Science* 37:737–761.

Zolensky M. E., Takenouchi A., Mikouchi T., Gregory T., Nishiizumi K., Caffee M. W., Velbel M. A., Ross D. K., Zolensky A., Le L., Imae N., and Yamaguchi A. 2020. The nature of the CM parent asteroid regolith based on cosmic ray exposure ages. *Meteoritics & Planetary Science* 56:49–55.

SUPPORTING INFORMATION

Additional supporting information may be found in the online version of this article.

Appendix S1. Raman-active modes of carbonate minerals and organic carbon.